

## Geomechanical paleostress inversion using fracture data<sup>☆</sup>

Laurent Maerten <sup>a,\*</sup>, Frantz Maerten <sup>a</sup>, Mostfa Lejri <sup>b</sup>, Paul Gillespie <sup>c</sup>

<sup>a</sup> Schlumberger, Parc PTP, 895 Rue de la vieille poste, 34000, Montpellier, France

<sup>b</sup> Schlumberger, 67 Albion Street, Leeds, LS1 5AA, UK

<sup>c</sup> Statoil, Forusbein 50, N-5035, Stavanger, Norway



### ARTICLE INFO

#### Article history:

Received 26 January 2016

Received in revised form

31 May 2016

Accepted 18 June 2016

Available online 23 June 2016

#### Keywords:

Paleostress

Inversion

Geomechanics

Faults

Fractures

### ABSTRACT

We describe a fast geomechanically-based paleostress inversion technique that uses observed fracture data to constrain stress through multiple simulations. The method assumes that the local stress field around individual fractures is heterogeneous and derives the far field tectonic stress, that we also call the far field boundary conditions. We show how such far field tectonic stress can be recovered through a mechanical stress inversion technique using local observations of natural fractures (i.e. mechanical type, orientation and location). We test the paleostress inversion against outcrop analogues of fractured carbonates from both Nash Point, U.K., where there are well exposed faults and joints and the Matelles, France, where there are well exposed faults, veins and stylolites. We demonstrate through these case studies how the method can be efficiently applied to natural examples and we highlight its advantages and limitations. We discuss how such method could be applied to subsurface problems and how it can provide complementary constraints to drive discrete fracture models for better fractured reservoir characterization and modelling.

© 2016 Elsevier Ltd. All rights reserved.

### 1. Introduction

The determination of the ancient state of stress in the earth's crust is of fundamental interest in tectonics and also forms the basis of detailed geomechanical modelling for industrial applications such as hydrocarbon exploration and production. In brittle tectonics, the most commonly applied techniques for paleostress inversion are based on the use of faults and their slip vectors estimated from slickenlines (e.g. Angelier, 1979, 1994). The majority of these techniques are founded on three assumptions (Nemok and Lisle, 1995):

1. Fault slip directions recorded from the slickenlines were parallel to the direction of resolved shear stress on the fault (the Wallace-Bott hypothesis);
2. Slip on the different faults was mutually independent;
3. The stress which induced slip on the faults can be considered homogeneous on a macroscopic scale.

The validity of these assumptions can be questioned (Dupin et al., 1993; Pollard et al., 1993; Nieto-Samaniego and Alaniz-Alvarez, 1995; Lisle, 2013) and in particular, assumption 2 is known to be incorrect for interacting faults (Maerten, 2000; Lejri et al., 2015; Maerten et al., 2016). In order to overcome these difficulties, we have developed a method of inversion of fracture data using elastic modelling in which faults are allowed to slip in any direction and they are allowed to geomechanically interact; thus assumptions 1 and 2 are no longer required. Furthermore the technique is extended to fractures with any mode of failure.

Numerical models of rock deformation based on continuum mechanics provide an efficient means for modelling natural fractures in reservoirs. Over the past decade, it has been shown that adding a geomechanical rationale to stochastic techniques improves their predictive capability and leads to more realistic fractured reservoir models (Maerten, 1999; Bourne et al., 2000). In areas that have not suffered previous deformation, pervasive or regional fracture systems may develop (Engelder and Geiser, 1980; Hancock and Engelder, 1989; Lorenz and Finley, 1991). However, where there are faults or folds that locally perturb the stress field, a fracture system with heterogeneous orientation and density may result (Rispoli, 1981; Pollard and Segall, 1987; Rawnsley et al., 1992; Maerten et al., 2002). According to the stress state and the rock mechanical properties, the fractures may be of differing fracture

\* This article is dedicated to the memory of Dr. Arnaud Etchecopar who passed away in February 2016.

\* Corresponding author.

E-mail addresses: lmaerten@slb.com (L. Maerten), fmaerten@slb.com (F. Maerten), mlejri@slb.com (M. Lejri), pgil@statoil.com (P. Gillespie).

mode, e.g. opening, closing or shearing mode.

The general concept for using geomechanical methods to predict natural fracture orientations, consists of calculating the stress distribution at the time of fracture initiation using the available reservoir structure data such as faults, fractures and folds, the rock type and the tectonic setting that can be characterized by stress or strain magnitude and orientation. The assumption that fractures are related to reservoir structure is not always valid, as fractures may predate or postdate the structure's formation and larger scale stress perturbations may not have any associated fracture arrays. The calculated stress fields, perturbed by the main structures are then combined with rock failure criteria and used to model natural fracture networks (i.e. orientation, and spatial density trends). A 2D illustration of the geomechanically-based method is shown in Fig. 1, in which a pre-existing discontinuity subjected to a load is sheared to create a fault. The stress is perturbed around the fault showing both tensile (light grey) and compressive areas (dark grey). Both  $\sigma_1$  (the most compressive principal stress) and the  $\sigma_2$  (the least compressive principal stress) are reoriented close to the fault. This stress pattern is compared to an outcrop example of reactivated pre-existing fractures (Fig. 1b and c) that shows branch cracks in areas of least compressive areas and stylolites in areas of highest compressive stress (Rispoli, 1981). The trajectories of the branch cracks and the stylolites follow the modelled orientation of  $\sigma_1$  and  $\sigma_2$  respectively.

Elastic geomechanics has been successfully applied to both outcrops and reservoirs demonstrating how geomechanics can help to predict natural fracture networks. For instance, the 3D boundary element method (BEM) has been successfully applied to model subseismic faults in highly faulted reservoirs in northern North Sea (Maerten, 1999; Maerten et al., 2006) as well as undetected joints in naturally fractured carbonate reservoirs (Bourne et al., 2000). Similarly elastic dislocation modelling has been applied to model small-scale fault and fracture network characteristics in normal and reverse fault regimes (Dee et al., 2007; Freeman et al., 2015).

Three key elements are essential for complete geomechanical modelling. The first element is the geological model, which constitutes the geometry of the subsurface geology. Although this is the most important element in geomechanical modelling, it is recurrently neglected because geological models are often oversimplified for technical and/or practical reasons. Geological models should resemble past and/or present day natural structures as far as possible. The second element is the tectonic stress, which comprises the type (normal, wrench or reverse), orientation and

magnitude of the regional or local tectonic stress through time. This element of the geomechanical modelling is the most difficult to evaluate and corresponds to the boundary conditions of the model. While there are techniques for measuring some components of the present day tectonic stress, it is not possible to directly measure past tectonic stresses. The stress field is often estimated by guess-work, introducing very high uncertainties in the stress modelling. Finally, the third element refers to the rock rheology. This element of the geomechanical modelling is the least uncertain. Thanks to laboratory testing we have a fair understanding of the rock mechanical properties. The rock properties at the time of deformation can be estimated using sensible assumptions about burial history, compaction and diagenesis (Laubach et al., 2009).

In this article we describe a method of stress inversion using observed structures, such as natural fractures, as input. While the basic principles of such techniques have been described in the past (Muller and Pollard, 1977; Baer and Reches, 1991; Maerten, 1999; Bourne and Willemse, 2001; Maerten et al., 2002; Homberg et al., 2004), here we extend the geomechanical stress inversion method described by Maerten et al. (2016) and used by Lejri (2015) and Abul Khair et al. (2015) to take into account such structures as input. The method is described and successfully tested against two different outcrop examples. To facilitate the reading, Table 1 defines all symbols used in this contribution.

## 2. Method

As early studies, using field observations and analytical models (Hafner, 1951; Couples, 1977; Pollard and Segall, 1987), predict that a heterogeneous stress field is caused by faulting, the proposed method concentrates solely on the case where faulting is the main driver for stress perturbation that would affect fracture development. This method then assumes that in a growing and active fault system, the orientation of fractures will be influenced by the regional tectonic stress as well as by the perturbation of that stress state by nearby larger faults. Consequently, we use geomechanical modelling to compute the heterogeneous stress around active faults through time and thereby model the orientation and density trends of the natural fractures.

Since the main unknown in such modelling is the boundary conditions applied to the geomechanical model in the form of the stress tensor, a theoretical workflow is set up such that it should help to recover, or at least better constrain, the paleo-tectonic stresses. First, a 3D model of the subsurface fault networks is

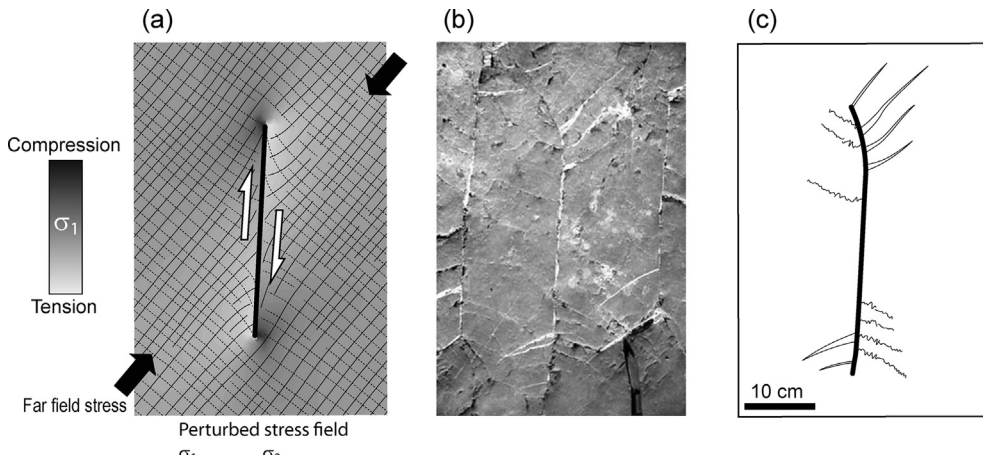


**Fig. 1.** Comparison between (a) stress perturbations computed around a single fault showing stress magnitude and orientation, (b) photo of secondary tensile cracks and stylolites observed around a reactivated fracture in limestone at Les Matelles, southern France (Rispoli, 1981; Petit and Mattauer, 1995) and (c) observed fracture interpretation of (b).

**Table 1**  
Symbol definitions.

Symbol	Comments
<i>Fault properties</i>	
$\delta$	Angle between $\sigma_1$ and fault plane
$\vec{n}$	Fault plane normal
<i>Rock properties</i>	
$\nu$	Poisson's ratio
$E$	Young's modulus
$\varphi$	Friction angle
<i>Stress</i>	
$\sigma_1 \geq \sigma_2 \geq \sigma_3$	Principal effective stress magnitudes (positive compression)
$\sigma_v$	Magnitude of the far field vertical stress
$\sigma_H$	Magnitude of the far field maximum horizontal stress
$\sigma_h$	Magnitude of the far field minimum horizontal stress
$\theta$	Orientation of $\sigma_H$ defined clockwise from the North
$R$	Stress ratio $R = (\sigma_2 - \sigma_3)/(\sigma_1 - \sigma_3)$
$\bar{R}$	Stress ratio defined by Maerten et al. (2014) for Andersonian regimes
<i>Acronyms</i>	
BEM	Boundary Element Method
FEM	Finite Element Method
DEM	Distinct Element Method
C	Mean cost
$C_{open}$	Cost for opening mode fracture
$C_{shear}$	Cost for shearing mode fracture
$C_{close}$	Cost for closing mode fracture

created. The model should honour, as far as possible, the interpreted 3D fault model. Then, thousands of geomechanical simulations are run covering the range of all possible Andersonian tectonic stresses in terms of orientation and magnitude. For each simulation, the modelled local heterogeneous stress field is compared with the observed natural fractures and it is checked whether such fractures could have been developed within the modelled stress field. Finally, all the simulation results are analysed in order to find the one that yields the best fit between modelled stresses and observed fractures. Once discovered, the optimum tectonic stress regime can then be used to constrain boundary conditions for forward geomechanical simulations that produce maps of potential fracture strike and density that in turn are used to constrain discrete fracture network models.

This idealized workflow for determination of the paleo-tectonic stress needs to be optimized using a proper 3D numerical method involving techniques to reduce both the computation time and to automatically derive the optimum solutions. The foundation of the proposed stress inversion technique, meant to optimize the idealized workflow and detailed in the next sections, is based on the principle of superposition (Brillouin, 1946 for review) to compute the stress at any location in the model using pre-computed specific values from three linearly independent simulations. This principle, combined with the 3D boundary element method (BEM) and a Monte Carlo procedure, is used to reduce the number of simulations needed for the inversion.

## 2.1. Numerical tool

The technology used for elastic geomechanical modelling can vary from the finite element method (FEM), distinct element method (DEM) to the boundary element method (BEM). We have chosen to use the BEM for four main reasons (Maerten et al., 2014): (i) complex and realistic fault models can easily be constructed as BEM uses frictional surfaces as 3D discontinuities (i.e. faults, joints, salt diapirs, bedding interfaces or cavities) in a homogeneous elastic medium that does not need to be discretized, (ii) discontinuity surfaces are made of triangular elements, which are particularly well suited to model complex surfaces such as a curving fault with irregular tip-line, (iii) computation is fast (i.e. several seconds

to few minutes) and (iv), as opposed to FEM, it is more convenient to impose a far field tectonic stress as it is independent of the orientation and geometry of the model edges (outer boundaries).

With that regards we have developed iBem3D (former Poly3D initially developed by Thomas, 1993), a numerical tool based on innovative iterative 3D BEM technology (Maerten et al., 2010, 2014; Maerten, 2010a). It is founded on the analytical solution for the elastic boundary value problem of an angular dislocation in an infinite "whole" space or semi-infinite "half" space composed of a homogeneous and isotropic linear-elastic material. One approximates rock mass of the upper crust as an elastic material. This elastic rock mass is cut by discontinuities (3D surfaces), which for instance, represent the geometry of the faults that have been interpreted from a seismic reflection survey. Only the boundary surfaces themselves are modelled, whereas the surrounding material need not be modelled explicitly. Modelled faults are discretized as triangular elements with specified constant displacement and/or traction boundary conditions. Fault friction, cohesion and fluid pressure can also be set as boundary conditions. Maerten et al. (2014) give an instructive summary of iBem3D technology as well as a list of published applications in the field of structural geology, fracture mechanics, geophysics, including applications to the oil and gas industry.

When modelling faults in the following paleostress inversion technique, the displacement component normal to the element plane is prescribed to be zero, to avoid opening and interpenetration of the fault walls. The initial two in-plane shear tractions on each element are set to be zero but are automatically determined and prescribed by remotely applied stresses. This fault boundary condition is essential if we want to use the reduced tensor for the paleostress inversion. Consequently, fault friction, cohesion and fluid pressure cannot be used during the inversion process. The underlying assumption is that this approximation is adequate to capture the first-order relationship between fault geometry, fault displacement distributions, and perturbed stress fields.

## 2.2. Fault paleo-geometry

To reduce geomechanical uncertainties associated with the geometry of the structure one must preserve the structural integrity

and complexity of the model. In a geomechanical simulation, a model of the present day observed geological structures is often used as proxy for past geometry. This is a good approximation for regions of normal faulting, where the local extension does not exceed 10–20%. However, for highly deformed areas such as fold and thrust belts, present day geometry cannot be used to model past deformation. In such cases, a thorough and well constrained 3D restoration of the geological structure has to be achieved in order to obtain a good estimate of the structural geometry through geological time.

### 2.3. Paleo-tectonic stresses

The main unknown for geomechanical simulations is the paleo-tectonic stress. It is always difficult to estimate paleo-tectonic stress in terms of both the orientation and the relative magnitude. In addition, calibration with available fracture data measured along wellbore for instance, is often time consuming as the process is not automatized. Thus this part of the process is often neglected and estimates of the paleo-tectonic stress are made without full use of available data.

We have therefore developed a new generation of paleostress analysis using iBem3D technology, which is an extension of the method of [Maerten et al. \(2016\)](#) for stress inversion from focal mechanisms, in which fracture data are used as the input. In principle, in order to recover paleo-tectonic stresses, thousands of simulations should be run, covering the range of all possible tectonic stress configurations. Then, for each simulation we compare attributes of the modelled stresses with the observed fracture geometry. Finally, the simulations that give the best fit with observed fracture data are selected. However, three main problems need to be solved in order to make the technique valuable: (i) the dimension of parameter space for covering the range of all possible tectonic stress configurations needs to be decreased, (ii) the computation time must be optimized and (iii), the analysis of the results must be automatic.

In addition, in order to determine which of the fractures to include in the paleo-tectonic stress inversion, we need to determine which of the available natural fractures are related to a particular past stress state and which are not.

#### 2.3.1. Parameter space

The full range of tectonic stresses is described by a 6 dimensional (6D) parameter space, which is related to the full symmetric stress tensor defined by:

$$\sigma = \begin{pmatrix} \sigma_{xx} & \sigma_{xy} & \sigma_{xz} \\ \sigma_{yy} & \sigma_{yz} & \sigma_{zz} \\ \sigma_{zz} & & \end{pmatrix} \quad (1)$$

However, in order to reduce computation time, we have reduced the parameter space to two dimensions.

We have assumed that one of the principal stress directions is vertical ([Anderson, 1905](#); [Lisle et al., 2006](#)). The 2D parameter space can therefore be defined by:

$$\sigma = \sigma(\theta, \bar{R}), \quad (2)$$

where  $\theta$  is the orientation of the maximum principal horizontal stress  $\sigma_H$  defined clockwise according to the north from  $0^\circ$  to  $180^\circ$  and  $\bar{R}$  the stress ratio for the three possible regimes, normal, wrench and reverse fault regimes ([Lejri et al., 2015](#)). The stress ratio  $\bar{R}$  is defined such that:

$$\left\{ \begin{array}{l} \text{Normal } \bar{R} = R \in [0, 1] \\ \text{Wrench } \bar{R} = 2 - R \in [1, 2] \\ \text{Reverse } \bar{R} = 2 + R \in [2, 3] \end{array} \right\} \quad (3)$$

$$\text{with } R = \frac{(\sigma_2 - \sigma_3)}{(\sigma_1 - \sigma_3)}, \quad (4)$$

Here, depending on which of the principal stresses is vertical, we can cover the normal, wrench and reverse stress regimes with  $\sigma_V = \sigma_1$ ,  $\sigma_V = \sigma_2$  and  $\sigma_V = \sigma_3$  respectively, using a single parameter that varies continuously from 0 to 3.

#### 2.3.2. Computation time

The key idea is to reduce the computation time using the principle of superposition ([Brillouin, 1946](#)), a well-known principle in linear elasticity. This allows recovery of the displacement, strain and stress at any observation point  $P$  using pre-computed specific values from three linearly independent simulations. This principle stipulates that a given value  $\sigma^t$  can be entirely determined by a linear combination of independent solutions such that:

$$\sigma^t = \sum_{i=1}^3 \alpha_i(\theta, \bar{R}) \sigma_i^t, \quad (5)$$

where  $\sigma^t$  is the tectonic stress,  $\alpha_i(\theta, \bar{R})$  are scalar coefficients and  $\sigma_i^t$  is the linearly independent pre-computed tectonic stresses.

Here, the 3 scalars  $(\alpha_1, \alpha_2, \alpha_3)$  are sufficient to cover the full range of tectonic stresses. Suppose that for each linearly independent tectonic stress  $\sigma_R^{(i)} \in [1, 3]$ , applied to a model, we compute and store the corresponding total stress tensor,  $\sigma_P^{(i)}$ , at a fracture location,  $P$ . Then, the total stress tensor at  $P$  due to the tectonic stress defined by  $\sigma_R(\alpha) = \sum \alpha_i \sigma_R^{(i)}$  ( $\alpha_i \in \mathbb{R}$ ) will be  $\sigma_P = \sum \alpha_i \sigma_P^{(i)}$ , involving only 18 multiplications. The total stress is defined as the imposed tectonic stress plus the perturbations caused by the slipping faults ([Crouch and Starfield, 1983](#)). As shown previously, any reduced Andersonian tectonic stress is entirely defined by only two parameters,  $\theta$  and  $\bar{R}$ . Although these two parameters are inverted, three simulations at initialization are required. The reason for this is that the components of the tectonic stress have to be used in the global coordinate system, i.e.,  $\sigma_{xx}$ ,  $\sigma_{xy}$  and  $\sigma_{yy}$ , in order to use the principle of superposition from linearly independent simulations. Using  $\theta$  and  $\bar{R}$  does not provide any linear relationship.

Using the principle of superposition does not require recomputing the unknown displacement discontinuities on triangular elements, making it possible to perform many simulations in few seconds (i.e. 50,000 in a couple of minutes). Therefore, if measurements of geological features are known at some given locations such as displacement, strain and/or stress, fractures orientation or secondary fault planes, which formed in the vicinity of major active faults, then it is possible to recover the triple  $(\alpha_1, \alpha_2, \alpha_3)$  and therefore the tectonic stress  $\sigma^t$  and the corresponding tectonic regime ([Maerten et al., 2016](#)).

#### 2.3.3. Fracture data and objective functions

We use a Monte Carlo method to find the parameters  $(\alpha_1, \alpha_2, \alpha_3)$ , which minimize some objective functions given three independent far field stresses. The objective functions must be as simple as possible in order to minimize computation time. We define the cost as the value of the objective function. In the present study we constrain the paleostress inversion exclusively with observed fracture data.

**2.3.3.1. Fracture data.** Three natural fracture types are defined (opening mode, closing mode and shearing mode fractures) based

on their development mechanism and their relationship with the orientations of the three principal stresses as described in Fig. 2.

Opening mode fractures form when the effective tensile stress in a direction perpendicular to the potential fracture plane reaches the tensile strength of the rock. Opening mode fractures show an extension perpendicular to the fracture walls. The most common opening mode fractures are the joints but veins (tension gashes) and dikes are also included (Pollard and Aydin, 1988). Opening mode fractures form in the plane perpendicular to the least compressive principal stress direction,  $\vec{\sigma}_3$ .

Closing mode fractures or anticracks (Fletcher and Pollard, 1981) form with a compressive stress in a direction perpendicular to the potential fracture plane. Closing mode fractures show a contraction perpendicular to the fracture walls. In clastic rocks at reservoir conditions, the most typical closing mode fractures are compaction bands (Mollema and Antonellini, 1996; Aydin et al., 2006). Closing mode fractures will form in a plane perpendicular to the most compressive principal stress direction,  $\vec{\sigma}_1$ . We also consider stylolites to be closing mode features even though they are non-elastic dissolution features. Nevertheless, we would expect stylolites peaks to initiate parallel to the most compressive principal stress direction.

Shearing mode fractures are generated by shear stress. A shearing mode fracture is a fracture along which the relative movement is parallel to the fracture walls. The most common kind of shearing mode fractures are faults and shear deformation bands (Aydin, 1978; Aydin et al., 2006). A shearing mode fracture is one of the two conjugate planes, oriented at acute angles  $\delta$  on either side of the most compressive principal stress direction,  $\vec{\sigma}_1$ , and with opposite sense of shear direction (see Fig. 2).  $\delta$  is defined according to the Coulomb criterion such that:

$$\delta = \frac{\pi}{4} - \frac{\varphi}{2}, \quad (6)$$

where  $\varphi$  is the angle of rock internal friction. We consider here the conjugate shearing mode based on Anderson (1905) application of the Mohr-Coulomb failure criterion, which assumes that shearing mode fractures form parallel to the intermediate principal stress direction,  $\vec{\sigma}_2$ . However, the proposed technique could easily be extended to polymodal shearing mode fractures (Donath, 1962; Aydin and Reches, 1982; Healy et al., 2006, 2015).

**2.3.3.2. Objective functions.** For a given tectonic stress defined by  $\theta$  and  $\bar{R}$ , the minimum cost for opening mode fractures,  $C_{open}$ , is such that the computed local minimum principal stress,  $\vec{\sigma}_3$ , is aligned with the normal  $\vec{n}$  of the observed opening mode fracture plane:

$$C_{open} = 1 - (\vec{\sigma}_3 \cdot \vec{n})^2 \quad (7)$$

In Equations (7)–(9), “.” represents the dot product. The dot product is squared as the normal can be on either side of the fracture plane.

For closing mode fractures, the minimum cost,  $C_{close}$ , is such that the computed local maximum principal stress,  $\vec{\sigma}_1$ , is aligned with the normal  $\vec{n}$  of the observed closing mode fracture plane:

$$C_{close} = 1 - (\vec{\sigma}_1 \cdot \vec{n})^2 \quad (8)$$

For shearing mode fractures, the minimum cost  $C_{shear}$  is such that the computed local minimum principal stress,  $\vec{\sigma}_3$ , is at angle  $\delta$  or  $-\delta$  (see Equation. (6)) from the normal  $\vec{n}$  of the observed shearing mode fracture plane. This can be expressed as  $(\vec{\sigma}_3 \cdot \vec{n})^2 = \cos^2 \delta = \frac{1}{2}(1 + \sin \varphi)$ , hence:

$$C_{shear} = \left| \left( \vec{\sigma}_3 \cdot \vec{n} \right)^2 - \frac{1}{2}(1 + \sin \varphi) \right| \quad (9)$$

The cost is normalized for the three fracture types and varies from 0 to 1. A cost of 0 means a perfect match between observed fractures orientation and local computed stresses, while a cost of 1 means the worst match. The three types of fractures can be combined and the total cost for one simulation will be the average cost of all observed fractures used to constrain the inversion. Each fracture data or data type can be weighted according to a user defined confidence criterion.

### 2.3.4. Tectonic stress domain

To better visualize and analyse the results of one paleostress inversion, which consists of thousands of simulations, we introduce the tectonic stress domain (Lejri et al., 2015), which is visualized on a 2D graph (Fig. 3) for which the x-axis is the stress ratio  $\bar{R}$ , and the y-axis is the orientation ( $\theta$ ) of the maximum horizontal stress relative to north. A point in the domain represents a single simulation; each simulation is coloured according to the computed cost which varies from 0 to 1. As we often have numerous observed fractures, the colour symbolizes the mean cost of all the fractures. For a given model, the inversion procedure will try to find the best solutions  $(\bar{R}, \theta)$  by minimizing the cost functions. These will be highlighted in the tectonic stress domain with appropriate colours (Fig. 3). The result of paleostress inversion is the optimum simulation (lowest cost), which includes the orientation and relative magnitude of the principal stresses as well as the stress regime (normal, wrench or reverse fault regime).

### 2.3.5. Under-constrained model

Depending on the model configuration and available fracture data, the paleostress inversion may be under-constrained. Under-constraint model configuration is not necessarily related to the number or quality of the available data but rather to the type of tectonic stress to be inverted or the kind of data used (fault model and fracture data).

The first under-constrained configuration is for stress ratios  $\bar{R} = 0$  and  $\bar{R} = 3$ , which correspond to radial extension (normal fault regime) and radial compression (reverse fault regime) respectively. Indeed, in such horizontal radial stress configurations, where  $\sigma_h = \sigma_H$ , the orientation of the maximum horizontal stress,  $\theta$ , is indeterminate.

The second under-constrained configuration is for a model with sub-vertical faults under an Andersonian state of stress, where displacement normal to the fault plane is not allowed and where

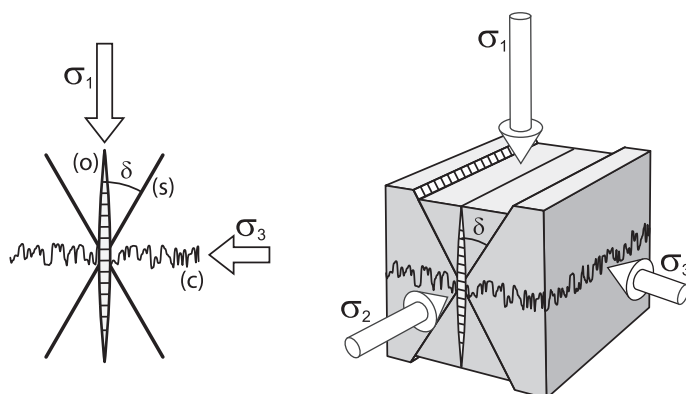


**Fig. 2.** Mechanical fracture types and relationship with principal stresses. (o) opening mode (i.e. joint), (c) closing mode (i.e. stylolite) and, (s) shearing mode (i.e. fault). Here, the stress does not need to be Andersonian with one principal stress being vertical.

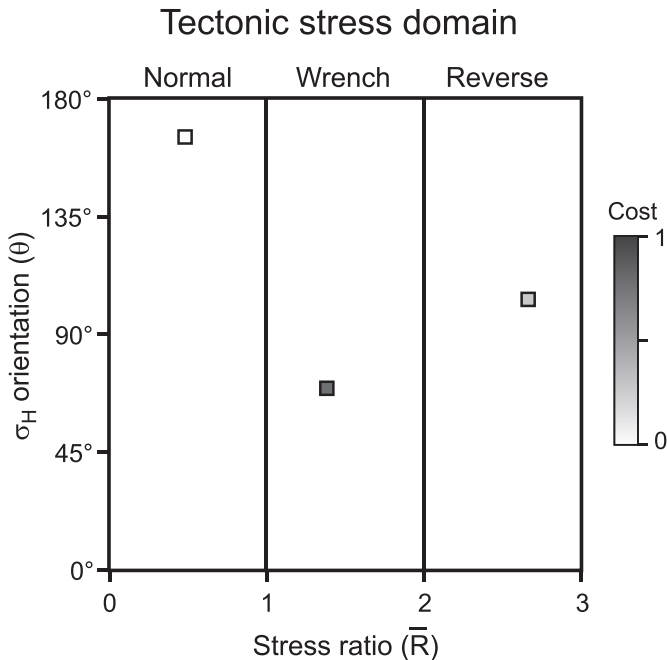


**Fig. 3.** Example of a tectonic stress domain. The x-axis is the stress ratio  $\bar{R}$ , and the y-axis is the orientation,  $\theta$ , of the maximum horizontal stress relative to north. A point in the domain represents one simulation that is coloured with respect to the computed cost which varies between 0 and 1.

frictionless slip is induced only by the two horizontal stresses  $\sigma_1$  and  $\sigma_H$ . This configuration produces uncertainty in finding  $\bar{R}$  and it can be demonstrated (see Appendix 1) that variation of the stress ratio  $\bar{R}$  or, in other words the ratio between the two horizontal stresses, will produce a pattern of stress trajectories around the sliding vertical faults identical to the stress trajectories for the same fault model under uniaxial compressive horizontal stress ( $\sigma_H$ ). This effect has previously been described by Bourne and Willemse (2001).

In our paleostress inversion simulations for both normal and wrench fault regimes, the opening mode fractures will be vertical (see Fig. 4i), so a model with sub-vertical faults and with observation of only vertical opening mode fractures will be under-constrained as it will be impossible to discriminate between  $\sigma_1$  being vertical (normal fault regime) or  $\sigma_2$  (wrench fault regime). In such case there will be an uncertainty in  $\bar{R}$  in both normal and wrench fault regimes as shown in the outcrop case studies of the next sections. A combination of vertical opening mode fractures and vertical closing mode fractures should constrain the inversion to the wrench fault regime (see Fig. 4i and ii), but  $\bar{R}$  will still be under-constrained. Similarly, for both wrench and reverse fault regimes, the closing mode fractures will be vertical (see Fig. 4ii), so a model with sub-vertical faults and observation only of vertical closing mode fractures will be under-constrained as it will be difficult to discriminate between  $\sigma_2$  being vertical (wrench fault regime) or  $\sigma_3$  (reverse fault regime). In this case there will be an uncertainty in  $\bar{R}$  in both wrench and reverse fault regimes.

### 3. Nash point outcrop case study

The study area is east of Nash Point, UK, on the northern margin of the Bristol Channel (longitude 3°33'W, latitude 51°24'N). Along this section, large coastal outcrops of the sub-horizontal Lower Jurassic (Liassic) sedimentary succession provide outstanding examples (Fig. 5) of strike slip faults and joints (opening mode

fractures).

#### 3.1. Nash point geological setting

Exposures along the beach east of Nash Point consist of interbedded lower Jurassic shallow marine pale grey limestone and marl. Individual layers, rarely greater than 1 m thick, are laterally continuous for up to 2 km except where faulted, and dip consistently to the south at less than 5°. The faults are conjugate strike-slip faults related to late Cretaceous to early Tertiary Alpine shortening (Peacock and Sanderson, 1992; Rawnsley et al., 1992; Nemčok et al., 1995). Faults display sub-horizontal striations with very small vertical offsets. Analysis of the regional unperturbed joint pattern consisting of parallel joints, yields an azimuth of maximum horizontal compression around  $170^\circ \pm 10^\circ$  (Petit et al., 2000).

The bedding plane joints exposed in the area have been described and partly mapped by Rawnsley et al. (1992, 1998) and Petit et al. (2000). Here we concentrate on the area (i) of Fig. 5 that we have carefully mapped from high quality air photos. The aerial photos are approximately true vertical photos that have been scaled, oriented and geo-referenced. In the vicinity of the faults, joints tend to be perturbed and are often sinuous with quite regular spacing. Fig. 6 shows the fault network of the studied area and the associated complex pattern of joints. Adjacent to the faults, joints become either parallel with or at high angle to the fault traces. This is particularly true around fault extremities (points A in Fig. 6), where the observed joint pattern resembles the pattern described in Fig. 1. At fault intersection showing acute angle (~35°), the joints tend to converge towards the fault intersections (points B in Fig. 6). Locally, joints converge towards points along some of the fault traces (points C in Fig. 6). These points of joint convergence were first described by Rawnsley et al. (1992).

The variability of the joints pattern at Nash Point clearly highlights the relationship between the strike slip faults and the development of the joints. While joints do not seem to be genetically linked to the faulting, they nonetheless appear to have developed within the perturbed stress field caused by slip along faults. The joint patterns at Nash Point, area (ii) of Fig. 5, have been previously modelled using photo-elastic models (Auzias, 1995; Rawnsley et al., 1997; Petit et al., 2000) as well as using 3D elastic dislocation model (Bourne and Willemse, 2001). These previous studies nicely demonstrate the mechanical relationship between the faults and the development of the joints.

#### 3.2. Nash point paleostress inversion

The first set of experiment consists of a paleostress inversion using a 3D model of the faults mapped in the area constrained with all the interpreted joints.

##### 3.2.1. Nash point model configuration

The 3D fault model (see Fig. 7) was built from the detailed interpretation of the fault traces in Fig. 6. The fault traces were vertically extruded in order to build sub-vertical faults with a height of 40 m (Rawnsley et al., 1998; Bourne and Willemse, 2001). A combination of traction and displacement boundary conditions was prescribed along each fault. A displacement component normal to the fault plane was initially set to 0 in order to prevent any opening or interpenetration of the fault walls. The two other components parallel to the fault plane, which may represent the local slip along a dip-slip or strike-slip fault, were set to have initial tractions (or stress drop) equal to 0 in order to let the faults freely slip in response to the remote load. These local boundary conditions allow for mechanical interaction between the faults.

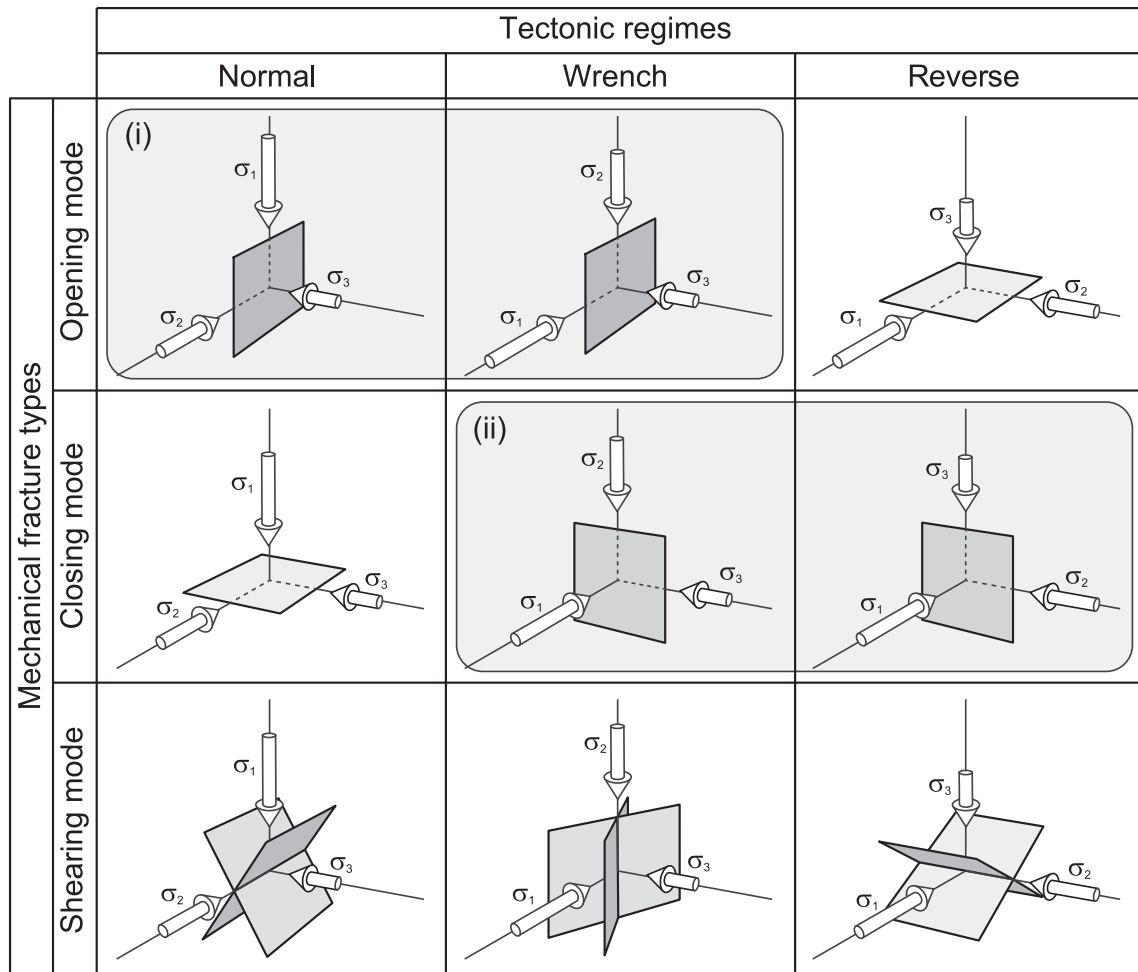


**Fig. 4.** Schematic figure showing the relationship between tectonic stress regimes and associated fracture types. (i) Under constrained configuration in the case of sub-vertical 3D fault model and sub-vertical opening mode fractures. Here there will be uncertainty in  $\bar{R}$  between normal and wrench fault regimes. (ii) Under constrained configuration in the case of sub-vertical 3D fault model and sub-vertical closing mode fractures. Here the uncertainty will be in  $\bar{R}$  between wrench and reverse fault regimes.

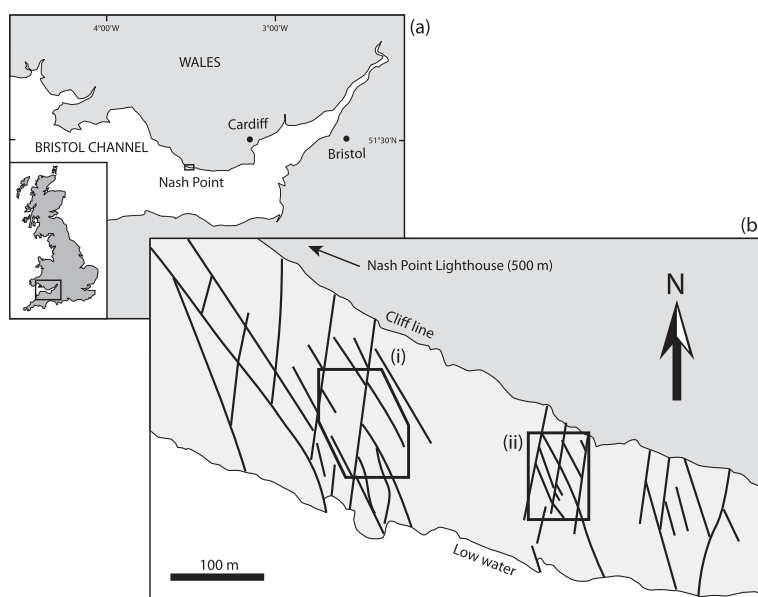


**Fig. 5.** (a) Location map and (b) mapped fault pattern of the Nash Point outcrop (modified from Petit et al., 2000). (i) Location of the studied faults and joints. (ii) Location of outcrop studied by Petit et al. (2000) and Bourne and Willemse (2001).

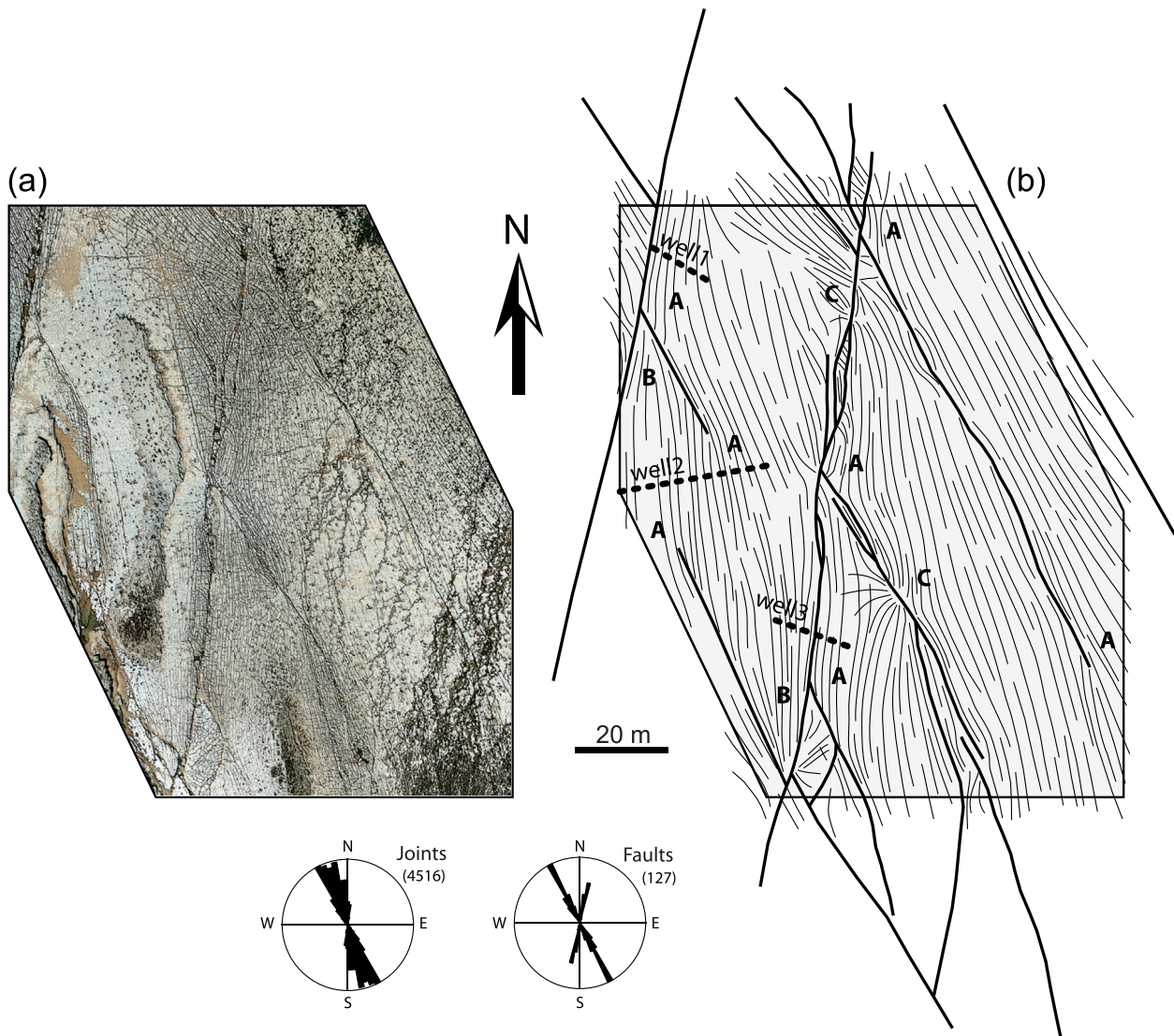


**Fig. 6.** Nash Point outcrop example. (a) Aerial photo of the area (photo courtesy of the Fault Analysis Group) and (b) interpretation showing joint pattern (thin black curves) and fault traces (thick black curves). Positions of fictitious wells are marked (dashed lines). Rose diagrams showing the strikes of joints and faults from the interpretation of the whole outcrop are also given.

In the following mechanical models we used a homogeneous whole elastic space with a linear elastic and isotropic behaviour characterized by two constants, Poisson's ratio and Young's Modulus. We used a value of 0.25 for Poisson's ratio ( $\nu$ ), 50 GPa for Young's Modulus ( $E$ ), which are the mean values representative for limestone (Clark, 1966). The paleostress inversion was constrained by the mapped joint traces (see Figs. 6b and 7) along which the dip angle ( $90^\circ$ ) and dip azimuth are known. The objective function used for the simulation is that described earlier for opening mode fractures and each datum was given equal weight. A layer parallel observation grid, covering the entire studied area, was used and placed at the mid height of the faults, which represents the sub-horizontal exposed bedding surface. These observation points, at which we compute the resulting perturbed stress field, are used to compare with the observed joint patterns.

### 3.2.2. Nash point model results

The paleostress inversion, which consists of 50,000 random geomechanical simulations, was run in less than 2 min. The optimum paleo tectonic stress found was oriented N163° ( $\sigma_H$ ) for a

mean cost  $\bar{C} = 0.0646$ . As anticipated, the corresponding tectonic stress domain (Fig. 8) shows that the model is under-constrained. Indeed, there is a strong uncertainty in  $\bar{R}$  that covers both the normal and wrench fault domain, which means that any stress fields with values of  $\bar{R}$  in the yellow zone (see Fig. 8) would give similar results.

Fig. 9 shows a qualitative comparison between the observed joint pattern and the model joint trajectories. Since joints (i.e. opening mode fractures) propagate in a surface normal to the local direction of the least compressive stress (i.e.  $\sigma_3$ ), the streamlines shown in Fig. 9b represent the strike of the plane containing  $\sigma_1$  and  $\sigma_2$ , which is mostly but not exclusively sub vertical in this case. The modelled joint trajectories (Fig. 9b) show a good correspondence with the observed joint pattern (Fig. 9a). Near the faults, the modelled trajectories become either parallel or at high angle to the fault traces as observed at points A around fault extremities and at fault intersections with an obtuse angle ( $\sim 145^\circ$ ). At fault intersections showing acute angle ( $\sim 35^\circ$ ), the modelled trajectories tend to converge towards the fault intersection points (points B). However, joint trajectories converging to points along some of the

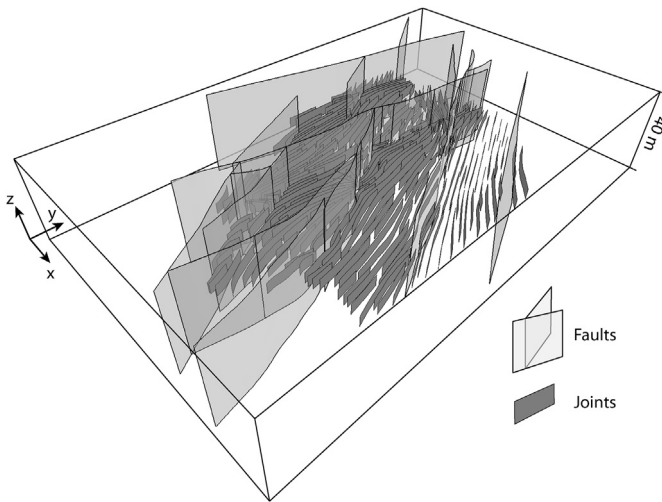


**Fig. 7.** Nash Point model configuration. 3D model made of sub-vertical faults and interpreted joints. Y-axis points to the North.

fault traces (points C in Fig. 6a and 9a) cannot be reproduced using the prescribed boundary conditions suggesting that other stress perturbation mechanisms are involved. These possible mechanisms will be discussed in a future article.

### 3.2.3. Nash point sensitivity to fracture data location

This section evaluates the extent to which the paleostress inversion is sensitive to the spatial distribution of fracture data used to constrain the inversion. The following paleostress inversion tests are summarized in Table 2 and include as constraining fracture data, (i) all the interpreted joints, (ii) all the interpreted joints minus those associated to local perturbations (joint trajectory convergence around points C), (iii) the joints from 3 synthetic wells taken individually, these 3 synthetic horizontal wells being located where the joints orientation are the most perturbed but away from local perturbations at points C (see Fig. 6b) and (iv), the joints from selected combinations of the 3 wells (well1 + well2, well2 + well3 and well1 + well2 + well3). Fig. 10 and Table 2 show the results of

these paleostress inversions.

The highest cost (i.e. the least constrained solution) is for the inversion constrained by all the joints. The orientation of  $\sigma_H$  found is  $N163^\circ$  and is similar to the mean joint strike or the inversion without any faults perturbing the stress. When the joint data used were cleaned of all the joints associated to local perturbations around points C, the orientation of  $\sigma_H$  found is still  $N163^\circ$  but the cost is significantly reduced (divided by 3.5), emphasizing the confidence in the inversion results. We therefore consider that  $N163^\circ$  is the best candidate for  $\sigma_H$  orientation and use it as a reference.

When the joint data taken from individual wells were used to constrain the inversion there was a discrepancy of  $10^\circ \pm 1^\circ$  in  $\sigma_H$  orientation with the mean joint strike. Furthermore,  $\sigma_H$  orientation derived from the mean joint strike is  $11^\circ$ – $20^\circ$  away from the reference  $N163^\circ$ . Among the 3 wells, Well 2 located between two mechanically interacting overlapping faults, gives a  $\sigma_H$  orientation similar to the reference. All the selected combinations of the 3 wells show that the inversion results always gives a  $\sigma_H$  orientation similar to or greater than the reference to a maximum of  $2.5^\circ$ , while the  $\sigma_H$  orientation derived from the mean joint strike is always greater than the reference by about  $15^\circ$ .

### 3.3. Nash point – discussion

The Nash Point case study is a very good example of fracture system (i.e. joints) that is not entirely dependent on the faulting, but where development and propagation was constrained by the stress perturbations caused by slip on nearby faults at the time of jointing. The joint density is almost constant while the joint trajectories clearly follow the stress trajectories. Performing paleostress inversion on the Nash Point data set is a special under-constrained case as the faults are sub-vertical. This leads to an uncertainty in finding the stress ratio  $\bar{R}$  as well as the tectonic regime. We are in the under-constrained configuration described in Fig. 4i. The optimum paleo tectonic stress found is oriented  $N163^\circ$  (orientation of  $\sigma_H$ ) which is in agreement with previous field observations (Rawnsley et al., 1998; Petit et al., 2000) and modelling studies (Auzias, 1995; Bourne and Willemse, 2001). This far field stress orientation imposed to the interpreted 3D sliding fault model creates a heterogeneous perturbed stress field that nicely matches most of the joint trajectories observed at Nash Point except locally where joint trajectories converge to points along the faults.

These results clearly illustrate that taking into account the stress perturbation around the faults is essential if we want to estimate the far field tectonic stress responsible for the joint development at Nash Point. It also highlights that, for reliable paleostress inversion, it is important to use fracture data scattered throughout the area of interest rather than a spatially concentrated high number of fracture data (Homberg et al., 1997).

## 4. Les Matelles outcrop case study

The second study area is located 15 km North of Montpellier, France, close to the village of Les Matelles. The exposure, located in a dry flat-bottomed valley (longitude  $3^\circ 48'E$ , latitude  $43^\circ 43'N$ ), is well suited for the study of brittle tectonics in limestone and stress perturbations around meso-scale faults (Rispoli, 1981; Petit and Mattauer, 1995; Soliva et al., 2010). Indeed, the exposure displays a large range of features including faults, stylolites, joints and veins filled with calcite.

### 4.1. Les Matelles geological setting

The exposure, situated along the Lirou fault, one of the splay

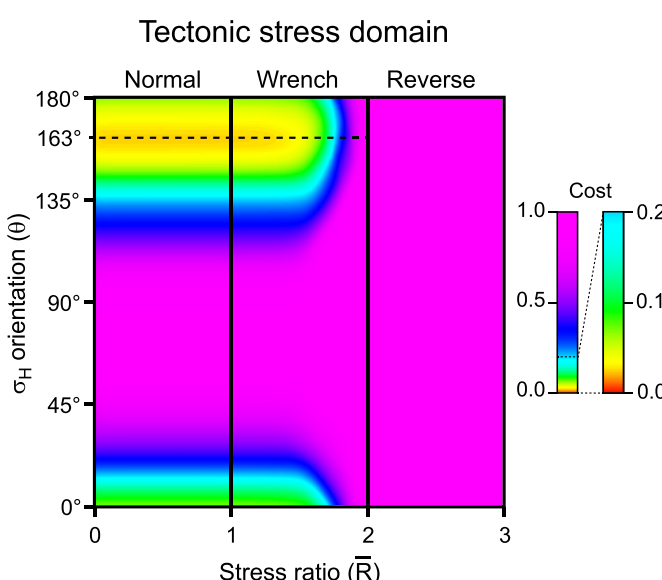


**Fig. 8.** Tectonic stress domain of the Nash Point inversion showing that the best maximum horizontal stress ( $\sigma_H$ ) is oriented  $163^\circ$ . The model is under-constrained resulting in a strong uncertainty in  $\bar{R}$ .

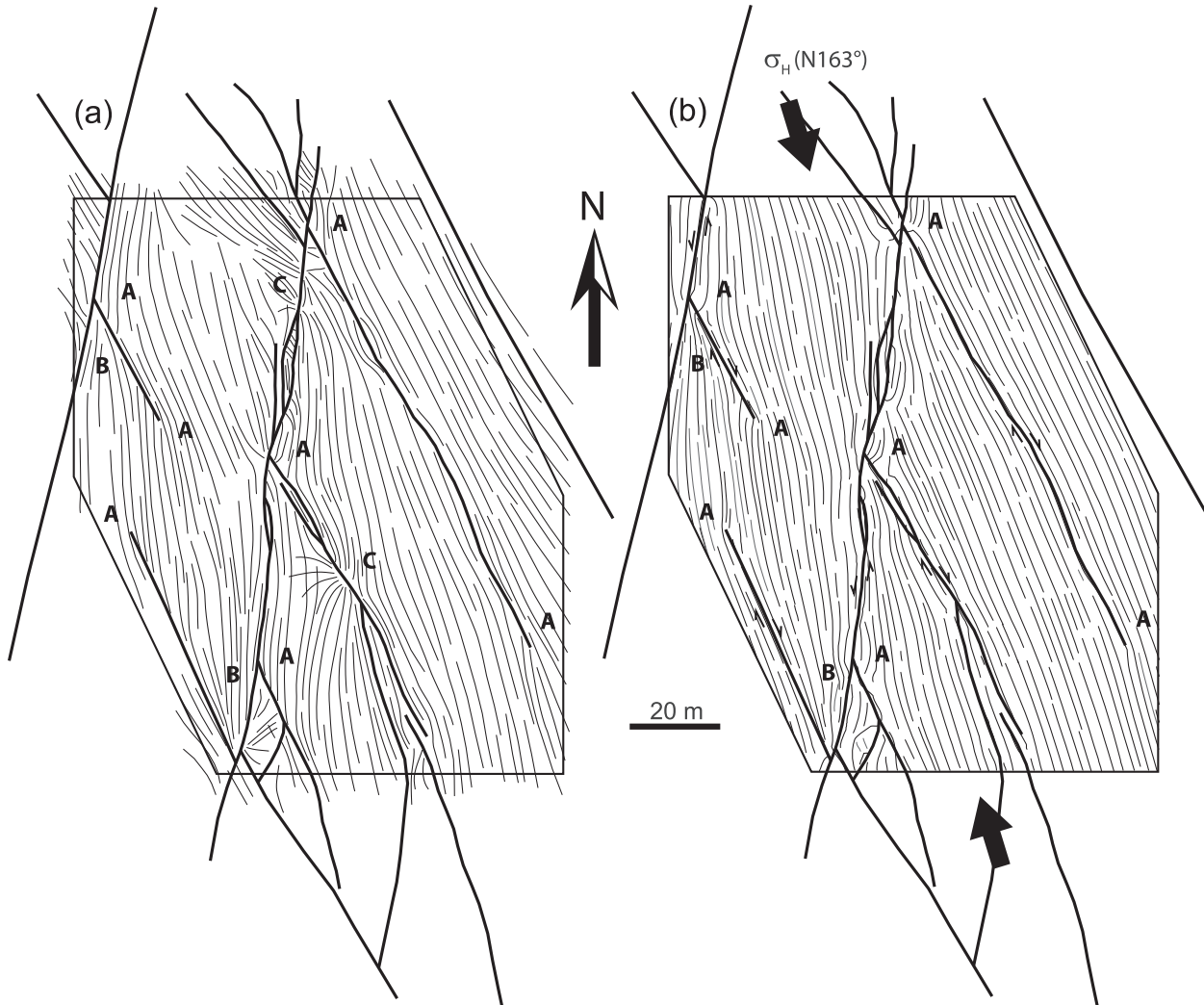


**Fig. 9.** Result of the Nash Point model. (a) Map of the observed joint pattern. (b) Map illustrating the modelled trajectories of the perturbed maximum horizontal stress,  $\sigma_H$  around faults (thick lines). Black arrows represent the orientation of the inverted regional  $\sigma_H$ . Points A, B and C, are described in the text.

**Table 2**

Fracture data used for the Nash Point case study.

	Fracture data	Fracture number	$\sigma_H$ orientation ( $\theta^\circ$ ) from mean joint strike	$\sigma_H$ orientation ( $\theta^\circ$ ) from inversion	Cost ( $\bar{C}$ )
1	All joints	4516	163.1	162.7	0.0646
2	All joints cleaned	3812	163.6	162.9	0.0181
3	Well1	7	184.7	174.2	0.0024
4	Well2	13	173.7	163.6	0.0016
5	Well3	12	182.3	173.2	0.0095
6	Well1 + well2	20	177.5	164.3	0.0041
7	Well3 + well2	25	177.8	165.0	0.0086
8	Well1 + well2 + well3	32	179.3	165.5	0.0082

faults of the Matelles fault, consists of very gently tilted ( $<10^\circ$ ) Jurassic micritic limestone layers. Individual layers, 20–30 cm thick, are laterally continuous along the Lirou valley for up to 200 m. Like most of the NE-trending faults bounding half-grabens north of Montpellier (see Fig. 11), the Matelles fault has been affected by two successive tectonic events: (i) a NS-trending contraction during the Pyrenean orogeny of Eocene age creating a left-lateral strike-slip movement and (ii), a SE-trending extension during the rifting of the Gulf of Lion passive continental margin of late Oligocene – early Miocene age creating a normal dip-slip

movement. Along the Lirou fault, these two successive events are evident from the presence of both sub-horizontal and dip-oriented slickenlines (Petit and Mattauer, 1995). The brittle tectonic structures observed on the exposure, those which have been described in a number of previous studies (e.g. Rispoli, 1981; Taha, 1986; Petit and Mattauer, 1995; Petit et al., 1999; Watkinson and Ward, 2006; Soliva et al., 2010), are of 3 types: long and straight faults, interpreted as reactivated joints, shorter and sinuous veins filled with calcite and stylolites. A detailed interpretation of these tectonic structures is proposed by Petit and Mattauer (1995). We therefore

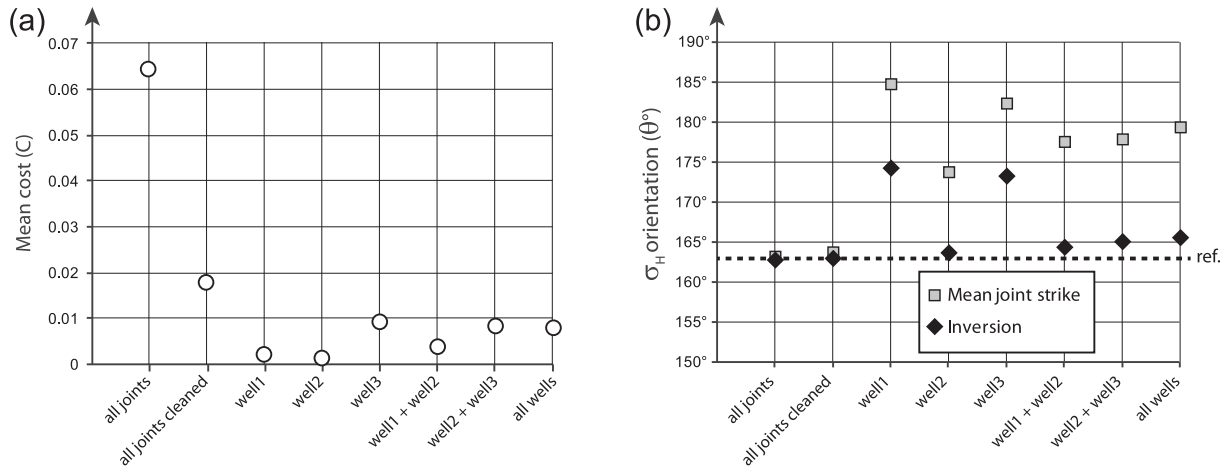


**Fig. 10.** Effect of fracture data location in the Nash Point model. (a) Graph showing the mean cost ( $C$ ) with respect to data location along wells and well combinations. (b) Graph showing both the inverted maximum horizontal stress ( $\sigma_H$ ) orientation (grey squares) and the mean joint strike (black diamond) with respect to data location along wells and well combinations. Dashed line represents the reference  $\sigma_H$  when using all fracture data.

base our analysis on their work in addition to our own field observations.

The fault pattern consists of a conjugate pair, a  $N20^\circ \pm 10^\circ$  trending left-lateral set and a  $N140^\circ \pm 10^\circ$  trending right-lateral set (Fig. 12). According to Petit and Mattauer (1995) these two sets are former joint sets that were reactivated during the latest compressive event. The maximum horizontal offset is 60 cm and is observed on one of the  $N20^\circ$  trending left-lateral faults. Horizontal offsets are generally smaller along the  $N140^\circ$  set than on the  $N20^\circ$  set.

The extensional fractures observed in the exposure are considered as veins because they contain often thick calcite fills. Their mean strike is  $N170^\circ \pm 10^\circ$  throughout the exposure, with local variation, and are almost always located either (i) around fault extremities (points A in Fig. 12b), where they follow the wing crack or horse tail pattern (Pollard and Segall, 1987; Granier, 1985), or (ii) at acute fault intersections showing, where they tend to converge towards the fault intersection points (point E in Fig. 12b) and (iii), at extensional jogs where they tend to be perpendicular to the overlapping fault traces (points C in Fig. 12b). The veins have a clear

genetic link with the faulting.

Two different sets of stylolites occur at the exposure. 1) A regular set occurring throughout the exposure oriented  $N55^\circ - 60^\circ$ . 2) A  $N100^\circ \pm 15^\circ$  trending set of stylolites, which is always superimposed on the earlier  $N55^\circ - 60^\circ$  set, is observed locally at contractional jogs along the  $N20^\circ$  faults (points B in Fig. 12b), at acute fault intersections (point E in Fig. 12a) and occasionally near fault tips (point D in Fig. 12b). Based on that observation, we infer that this set of stylolites is genetically linked to the faulting. Similarly, the nearly  $N50^\circ$  trending dense stylolites observed between the two parallel  $N140^\circ$  faults in the northern part of the exposure could be attributed, at least partly, to the stress reorientation guided by the reactivation of the  $N140^\circ$  joints during the shortening event. All of the stylolites have peaks sub-perpendicular to the stylolite surfaces and can therefore be interpreted as anti-cracks (Fletcher and Pollard, 1981) formed perpendicular to the most compressive stress.

The brittle deformation sequence described by Petit and Mattauer (1995) began by two successive jointing stages of the

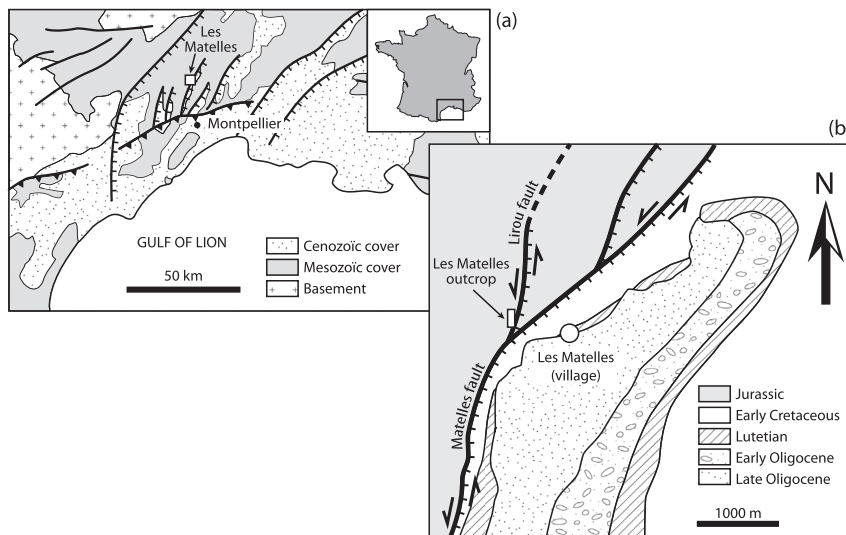


**Fig. 11.** Location and geological context of the Matelles study area. (a) Regional structural scheme of the study area. (b) Structural sketch map showing the geological setting of the Matelles Fault and the Lirou fault splay, with location of the presented outcrop (from the 1:50,000-scale geological maps of Montpellier and Saint Martin de Londres).

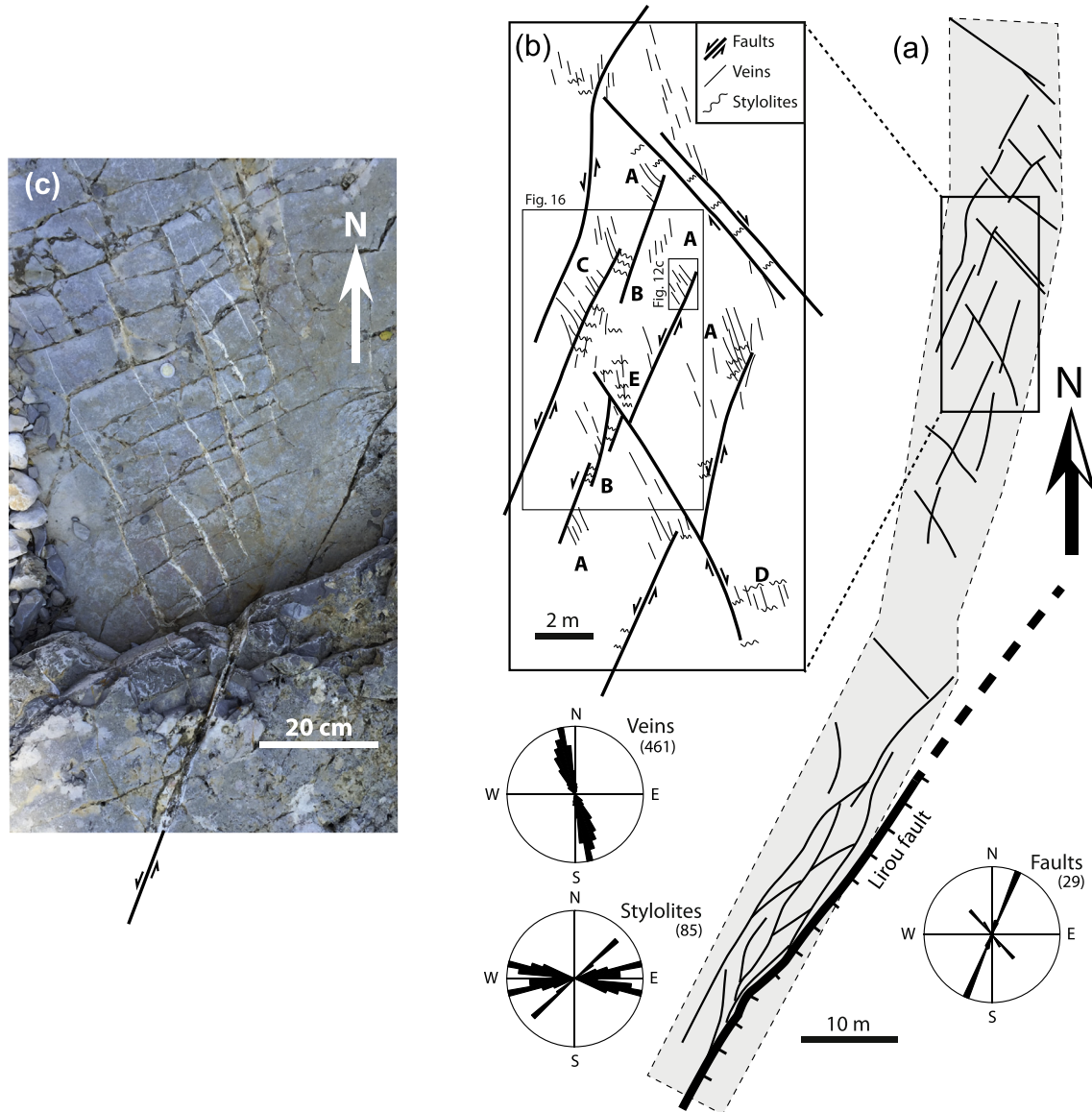


**Fig. 12.** Interpreted fractures at the Matelles outcrop. (a) Map of the main faults in the footwall of the Lirou fault. (b) Detailed map of mesoscale structures used for the simulation. Rose diagrams showing the strikes of veins, stylolites and faults from the interpretation of the studied outcrop are also given. The maps are modified from [Petit and Mattauer \(1995\)](#). (c) Photograph of a strike-slip fault termination showing tail cracks (veins). Its location is on [Fig. 12b](#).

Jurassic limestone layers with two principal trends, N20° and N140°. In the third stage, the first generation of stylolites were developed, oriented N55°–60° (not represented in Fig. 12b). The fourth stage, which is the one that we consider in the following simulations, was the final shortening event in which there was the reactivation of the previous structures as both left-lateral and right-lateral strike slip faults with associated wing cracks, *en échelon* veins and a second generation of stylolites around the reactivated joints.

#### 4.2. Les Matelles paleostress inversion

##### 4.2.1. Les Matelles model configuration

The 3D fault model (see Fig. 13) was built from the interpretation of the fault traces (Fig. 12b). The fault traces were vertically extruded in order to build a sub-vertical fault model with a height of 3 m, which is the greatest vertical size observed in the exposure. The same combination of traction and displacement boundary

conditions is used as in the Nash Point case study, allowing for mechanical interaction between the faults (see Section 3.2.1).

In the following mechanical models a homogeneous whole space with a linear elastic and isotropic behaviour is used. It is characterized by two constants, Poisson's ratio and Young's Modulus for which the values are similar to the Nash Point case study. The paleostress inversion was constrained by both the mapped vein and the stylolite traces (see Fig. 12) along which the dip angle (90°) and dip azimuth are known. The objective functions used for the simulation are those for both the opening mode and the closing mode fractures described earlier. A layer parallel observation grid, covering the entire studied area, was used and was placed at the mid height of the faults. The resulting perturbed stress field, computed at observation points along the observation grid, was compared with the observed joint patterns.

##### 4.2.2. Les Matelles model results

The paleostress inversion, which consists of 50,000 random

geomechanical simulations, was run in less than 30 s. The optimum paleo tectonic stress found is also oriented N163° ( $\sigma_H$ ) for a mean cost  $\bar{C} = 0.0361$ . The corresponding tectonic stress domain is displayed (Fig. 14). The uncertainty in  $\bar{R}$  is restricted to the wrench fault domain and the best solution is given for  $\bar{R} = 1.45$ . Even though the Matelles model is very similar to the Nash Point example with sub-vertical faults, it is much less under-constrained. Indeed, adding a second type of mechanical fracture, such as the sub-vertical stylolites (closing mode fractures), reduces the uncertainty in the paleostress inversion in the  $\bar{R}$  domain.

Fig. 15 shows a qualitative comparison between the observed fractures and the modelled trajectories of the same fractures based on the computed stress tensor. Since veins (i.e. opening mode fractures) propagate in a surface normal to the local direction of the least compressive stress (i.e.  $\sigma_3$ ), the streamlines shown in Fig. 15a represent the strike of the plane containing  $\sigma_1$  and  $\sigma_2$ , which is mainly sub-vertical in this case. Similarly, as stylolites propagate in the surface normal to the local direction of the most compressive stress (i.e.  $\sigma_1$ ), the streamlines (Fig. 15b) represent the strike of the plane containing  $\sigma_2$  and  $\sigma_3$ , which is also mainly sub-vertical. Fig. 15c represents the mean stress, and is used here to illustrate the zones that underwent more or less compression and that can be related to the location and density of observed stylolites and veins respectively. The modelled fracture trajectories show a good correlation with the observed fracture patterns.

Observed veins are almost exclusively located in areas of computed low compressive stress as occurs in extensional jogs (point C see Fig. 15a,c), where veins become perpendicular to the overlapping fault traces, and around fault tips (points A in Fig. 15a,c), where veins tend to be at high angle to the fault traces and form a horse tail pattern. Similarly, stylolites are concentrated in areas of computed higher compressive stress as occur in contractional jogs (points B in Fig. 15b,c), where stylolites become perpendicular to the overlapping fault traces, and at acute fault intersections, where they tend to be perpendicular to the acute bisector (point E in Fig. 15b,c). The modelled vein trajectories of Fig. 15a are analogous to the  $\sigma_1$  trajectories as  $\sigma_2$  is typically vertical (cf. Fig. 10 of Petit and Mattauer, 1995).

The geomechanical simulation shows that the maximum horizontal offset along the faults is on the N20° trending fault set. The N140° fault set yields a computed average maximum slip magnitude about 25% less than that of the N20° fault set. This is in agreement with the observation made by Petit and Mattauer (1995). For a frictionless model, the N140° trending faults are indeed less optimally oriented for slip with respect to the N163°

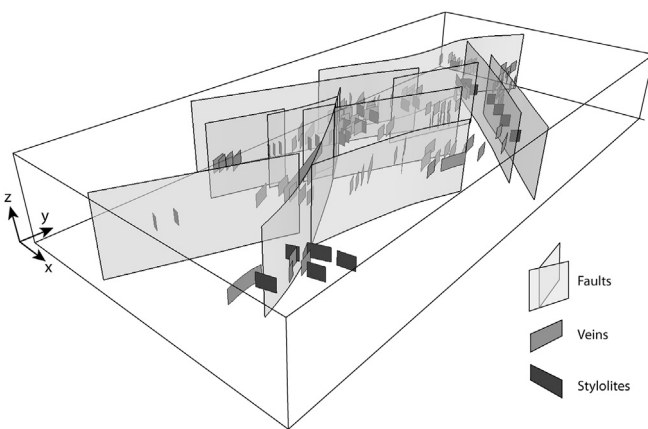


Fig. 13. The Matelles model configuration. 3D model made of sub-vertical faults and interpreted veins and stylolites. Y-axis points to the North.

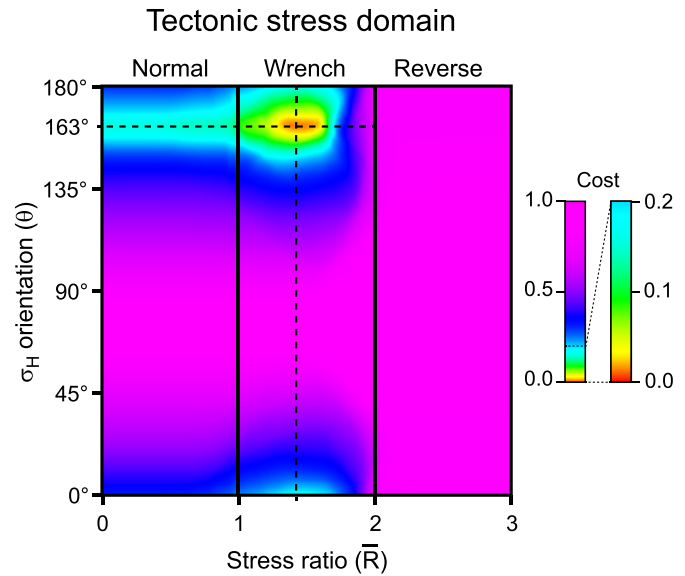


Fig. 14. The Matelles paleostress inversion results. Tectonic stress domain of the Matelles inversion showing that the best maximum horizontal stress ( $\sigma_H$ ) is oriented 163°.

direction of  $\sigma_H$  than the N20° set. This also highlights that the two sets of faults are not likely to have initiated as coeval conjugate sets, as suggested by Rispoli (1981), but rather formed as two sets of pre-existing fractures that were reactivated, as proposed by Petit and Mattauer (1995).

#### 4.2.3. Les Matelles sensitivity to 3D fault model geometry

Here we want to evaluate the effect of the 3D fault model geometry, which perturbs the stress field, on the paleostress inversion results. The following test is not an exhaustive analysis but rather serves as a representative example. For this test we concentrate on the local area described in Fig. 12b and we changed the 3D fault model geometry by removing the two overlapping faults (see Fig. 16b), which create both extensional and contractional jogs with associated veins and stylolites. The same model parameters are used for the paleostress inversion except that we exclusively use the veins and stylolites observed in the contractional relay of the two missing faults (bold black features in Fig. 16) to constrain the inversion. The first results displayed on Fig. 16a are for a complete fault model. We obtain N164° for orientation of  $\sigma_H$  and 1.44 for  $\bar{R}$ , which are very close to the previous model (N163°,  $\bar{R} = 1.45$ ), but with a lower mean cost  $\bar{C} = 0.013$ . This demonstrates the consistency of the paleostress inversion when less fracture data are used for the same 3D fault model. The second results displayed on Fig. 16b are for the altered 3D fault model, where the two faults have been removed. As opposed to the previous test, we do not obtain the same orientation of  $\sigma_H$  (N003°) and  $\bar{R}$  (1.49) for a higher mean cost ( $\bar{C}=0.031$ ). This means that in such conditions it is more difficult to find a good solution. This is qualitatively highlighted in Fig. 16b, where we can see that most of the observed meso-scale structures (i.e. veins and stylolites) in the area of interest cannot be matched with the modelled trajectories.

#### 4.3. Les Matelles – discussion

In contrast to Nash Point, the Matelles case study is an example of structures (i.e. veins and stylolites) that are genetically linked to the faulting. The fracture density is heterogeneous and always

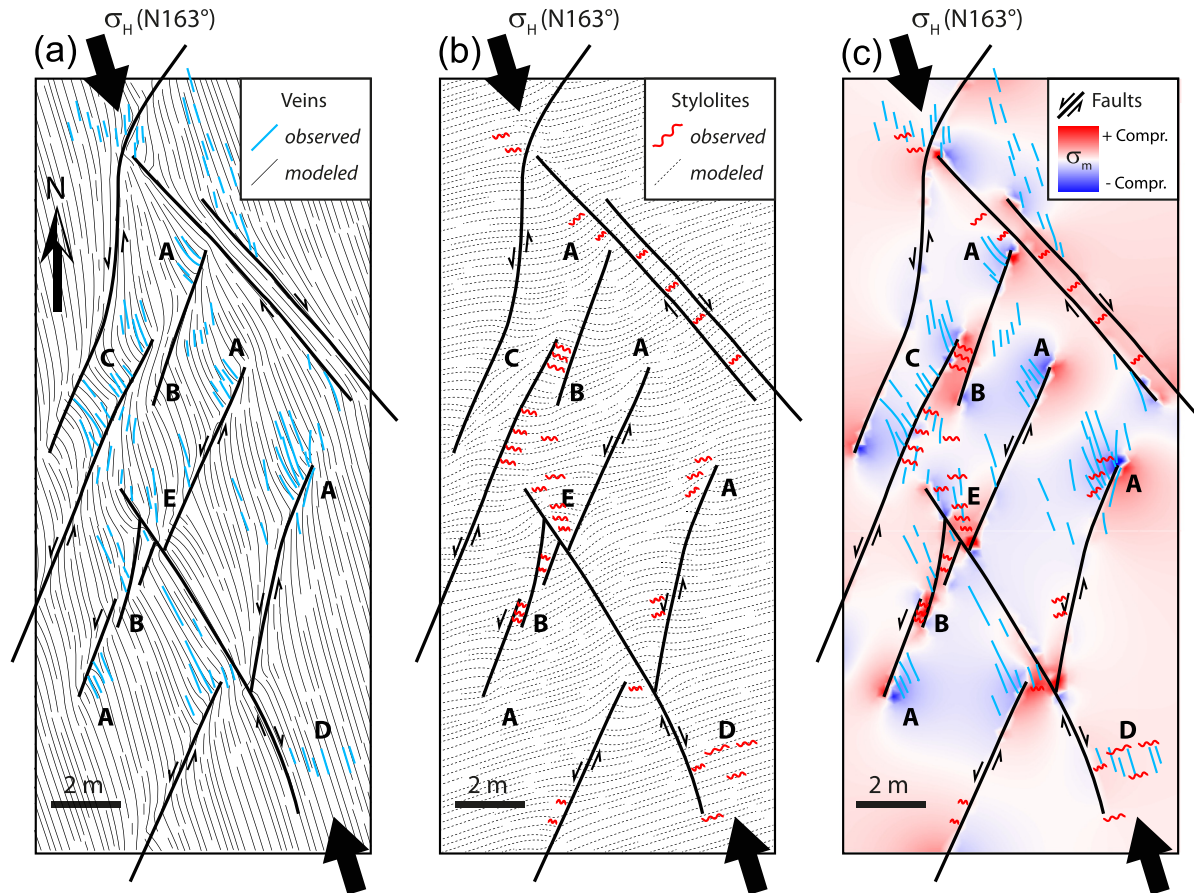


**Fig. 15.** Result of the Matelles model. (a) Map illustrating the modelled trajectories of the veins around faults. (b) Map illustrating the modelled trajectories of the stylolites around faults. (c) Map of the modelled mean stress illustrating areas of more or less compression that can be linked to the observed mesoscale structures.

located near fault extremities or at contractional or extensional relays, suggesting that their development was conditioned by the faulting. Even though the Matelles faults are sub-vertical, the model is less under-constrained than the Nash Point model because we have combined two types of fractures (i.e. opening and closing mode fractures). The optimum paleo tectonic stress found is strike-slip stress regime oriented N163° (orientation of  $\sigma_H$ ), which is in agreement with previous field observations (Petit and Mattauer, 1995). This far field stress orientation imposed on the interpreted 3D sliding fault model creates a heterogeneous perturbed stress field that matches most of the observed fractures trajectories and locations observed at the Matelles outcrop.

We have shown that the paleo stress inversion is very sensitive to the 3D fault model geometry. Omitting faults in the simulation could have a pronounced impact on the results, both in terms of far field paleo tectonic stress and local stress perturbations. If the Matelles example is scaled-up to the size of a hydrocarbon reservoir, Fig. 16 nicely highlights that if the only available fractures from observation are located near missing faults, then the modelled fracture characteristics (i.e. type orientation and location) can be far from reality and potentially have a great impact on the following flow simulation results.

## 5. Conclusions

We have demonstrated that it is possible to reduce uncertainty in the paleo-tectonic stress characteristics (style, orientation and relative magnitude) needed to efficiently constrain geomechanical

simulations used for modelling natural fractures in the subsurface. This is done using the mechanically-based paleostress inversion developed by Maerten (2010b); (Maerten et al., 2016). The method is based on the principle that any large scale rock discontinuities such as faults, salt bodies, décollement layers or cavities, subjected to far field stresses, generate local stress perturbations that in turns can be the drivers for the development of secondary structures such as smaller scale fractures. Knowing the location and characteristics of these natural fractures as well as the kind and geometry of the large scale discontinuities, should be sufficient to recover the far field stress responsible for the development of the smaller scale fractures. Therefore, the method depends upon the assumption that, for instance, in a growing and active fault system, the orientation of natural fractures are influenced by the regional tectonic stress as well as by the perturbation of that stress state by nearby active larger faults.

Unlike most paleostress inversion techniques, which are mainly based on measured fault slip data, our method takes into account any type of observed and measured deformation that is associated with a local stress state. We have demonstrated that the three mechanical fracture types, opening, closing and shearing mode fractures, can be efficiently used to constrain the paleostress inversion. In the case of well data, it is not possible to observe slickenlines in borehole imagery and oriented slickenline data are seldom available from core. Using the new technique it is possible to invert for the stress even in such cases where there are no kinematic indicators. In addition, the proposed method takes into account the heterogeneous state of stress that can be found around

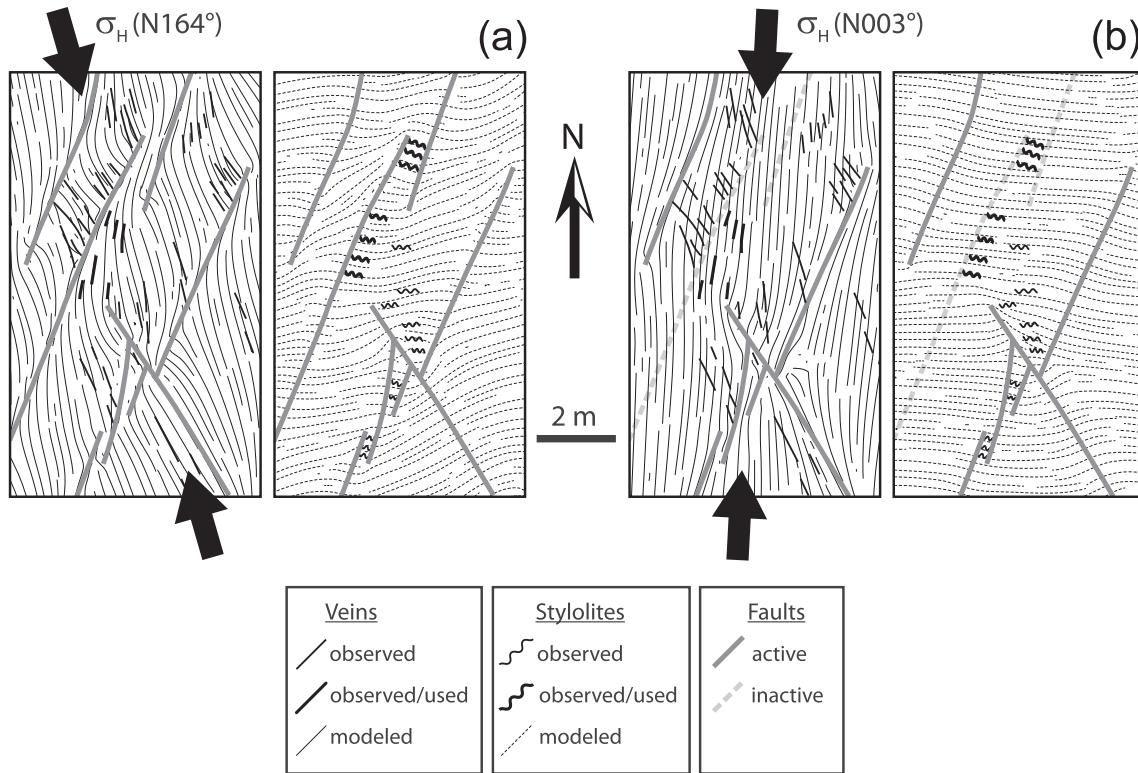


**Fig. 16.** Sensitivity to fault model geometry. (a) Model results using all the interpreted faults. (b) Model results using incomplete fault model. The dashed faults represent the missing faults. In both simulations, the veins and stylolites used to constrain the inversion are in bold.

active faults, which is not the case of the commonly used paleostress inversion techniques.

The linear elastic assumption used in the proposed method might seem too restrictive. Indeed, non-linear behaviour such as plasticity is not considered here. However, this linear elastic assumption appears nonetheless adequate to explain most of the observed brittle natural deformation in the natural examples. In addition, the assumption of linear elasticity provides the advantage that the principle of superposition can be used, allowing for very fast and efficient computation.

We have found configurations where the model (3D fault pattern and fracture data) used to constrain the paleostress inversion is under-constrained. For instance a sub-vertical fault model with associated vertical fractures can lead to uncertainty in finding the tectonic regime and the stress ratio  $\bar{R}$ . Another under-constrained class of model is represented by fracture data that are not well enough spatially distributed around the active faults. In this case, the paleostress result can be uncertain in both  $\bar{R}$  and  $\theta$ , as there may be several different stress regimes that could explain the fracture observations.

We have demonstrated that the fault model geometry is critical for the proposed technique. Therefore, preservation of a model's structural integrity and complexity is important and a realistic 3D geological model has to be carefully built. As knowledge of the 3D fault geometry is not always available from outcrop observations, the use of the method seems to be better suited to subsurface observations such as those available in the oil and gas industry, where seismic reflection and well data provide input for building realistic 3D models of the geological structure.

The stress inversion method is difficult to apply in cases where the fracture data were developed during multiple tectonic phases and where the mechanical type of the fractures is not known. In

both cases a tedious manual typing and sorting of the fracture data is necessary to test several tectonic hypotheses (Lejri, 2015).

Finally, the input data are not limited to fracture data. The paleostress inversion can be constrained by any data that record the deformation and/or the stress state around active faults. Therefore, we could define cost functions for a large variety of dataset used to constrain the inversion such as in-situ stress (breakout, leak off tests, induced fractures, well bore ovalisation), fault throw, slick-line, GPS, InSAR, tiltmeter, focal mechanism, micro-seismicity and deformed horizons (Maerten, 2010b; (Maerten et al., 2016)). These data, if appropriate, could of course be combined during the inversion.

## Acknowledgments

We would like to thank Jean-Pierre Joonekindt, Alvaro Gonzalez, Patxi Lahetjuzan, Emmanuel Malvesin and Fabrice Levassor for their support during this work. Simmons Aerofilms are thanked for producing aerial survey of the Nash Point area as well as the Fault Analysis Group for letting us exploit the air photos. Jean-Pierre Petit is thanked for providing us with his detailed fracture maps of the Matelles outcrop and Roger Soliva for guidance in the field. Finally, Clare Bond, Steve Laubach and Toru Takeshita are thanked for their constructive and thoughtful reviews. This study is part of M. Lejri's PhD thesis, funded by both the French Ministry of Research and Schlumberger and granted by the University of Montpellier. These organisations are gratefully acknowledged.

## Appendix 1

For a vertical frictionless fault constrained by an Andersonian state of stress and for which the normal displacement to the fault

plane is not allowed, it can be shown that the induced stress trajectories around the slipping fault are independent of the horizontal stress ratio and are similar to those of the same model subjected to uniaxial compressive horizontal stress.

If the vertical planar fault is defined by its normal  $\vec{n}(x, y, 0)$  with  $x^2 + y^2 = 1$ , then, for a given applied far field stress  $\sigma = \begin{bmatrix} \sigma_h & & \\ & \sigma_H & \\ & & \sigma_v \end{bmatrix}$ , the resolved traction on the fault plane is  $\vec{t} = \sigma \cdot \vec{n} = \begin{cases} x\sigma_h \\ y\sigma_H \\ 0 \end{cases}$ .

The shear traction is given by

$$\begin{aligned} \vec{t}_s &= \vec{t} - \vec{t}_n = \begin{cases} x\sigma_h - x(x^2\sigma_h + y^2\sigma_H) \\ y\sigma_H - y(x^2\sigma_h + y^2\sigma_H) \\ 0 \end{cases} = \\ &= \begin{cases} -xy^2(\sigma_H - \sigma_h) \\ yx^2(\sigma_H - \sigma_h) \\ 0 \end{cases} = (\sigma_H - \sigma_h) \begin{cases} -xy^2 \\ yx^2 \\ 0 \end{cases}. \end{aligned}$$

Consequently, the components of the resolved shear traction vector are proportional to  $(\sigma_H - \sigma_h)$ . When changing the magnitude of the horizontal principal stresses, the resolved shear traction is uniformly scaled but the direction and sense do not change. As a result, in a homogeneous and isotropic elastic medium, the resulting slip vector on the fault plane will be scaled accordingly and the perturbed stress around the slipping fault will be scaled as well. That is to say, the magnitudes of the displacement and stress field will be scaled uniformly, but the orientations will be the same.

## References

- Abul Khair, H., Cooke, D., Hand, M., 2015. Paleo stress contribution to fault and natural fracture distribution in the Cooper Basin. *J. Struct. Geol.* 79, 31–41.
- Anderson, E.M., 1905. The dynamics of faulting. *Trans. Edinb. Geol. Soc.* 8 (3), 387–402.
- Angelier, J., 1979. Determination of the mean principal directions of stresses for a given fault population. *Tectonophysics* 56, T17–T26.
- Angelier, J., 1994. Fault slip analysis and paleostress reconstruction. In: Hancock, P.L. (Ed.), *Continental Deformation*. Pergamon Press, Oxford, pp. 53–100.
- Auzias, V., 1995. Contribution à la caractérisation tectonique des réservoirs fracturés. Ph.D. thesis, Université Montpellier II.
- Aydin, A., 1978. Small faults formed as deformation bands in sandstone. *Pure Appl. Geophys.* 116, 913–930.
- Aydin, A., Borja, R.I., Eichhubl, P., 2006. Geological and mathematical framework for failure modes in granular rock. *J. Struct. Geol.* 28, 83–99.
- Aydin, A., Reches, Z.E., 1982. Number and orientation of fault sets in the field and in experiments. *Geology* 10 (2), 107–112.
- Baer, G., Reches, Z., 1991. Mechanics of emplacement and tectonic implications of the Ramon dike systems, Israel. *J. Geophys. Res.* 96, 11,895–11,910.
- Bourne, S.J., Rijkels, L., Stephenson, B.J., Willemse, E.J.M., 2000. Predictive modeling of naturally fractured reservoirs using geomechanics and flow simulation. *GeoArabia* 6, 27–42.
- Bourne, S.J., Willemse, E.J.M., 2001. Elastic stress control on the pattern of tensile fracturing around a small fault network at Nash Point, UK. *J. Struct. Geol.* 23, 1753–1770.
- Brillouin, L., 1946. *Wave Propagation in Periodic Structures: Electric Filters and Crystal Lattices*. McGraw-Hill, New York.
- Clark Jr., S.P. (Ed.), 1966. *Handbook of Physical Constants (Revised Edition)*. Geological Society of America Memoirs 97.
- Couples, G., 1977. Stress and shear fracture (fault) patterns resulting from a suite of complicated boundary conditions with applications to the wind river mountains. *Pure Appl. Geophys.* 115, 113–133.
- Crouch, S.L., Starfield, A.M., 1983. *Boundary Element Methods in Solid Mechanics: With Applications in Rock Mechanics and Geological Engineering*. Allen and Unwin Ltc, Winchester, Mass.
- Donath, F.A., 1962. Analysis of Basin-Range structure, south-central Oregon. *Geol. Soc. Am. Bull.* 73 (1), 1–16.
- Dupin, J.M., Sassi, W., Angelier, J., 1993. Homogeneous stress hypothesis and actual fault slip: a distinct element analysis. *J. Struct. Geol.* 15, 1033–1043.
- Dee, S.J., Yielding, G., Freeman, B., Healy, D., Kusznir, N.J., Grant, N., Andellis, P., 2007. Elastic dislocation modelling for prediction of small-scale fault and fracture network characteristics. In: Lonergan, L., Jolly, R.H., Rawnsley, K., Sanderson, D.J. (Eds.), *Fractured Reservoirs*. Geological Society of London, vol. 270. Special Publication, pp. 139–155.
- Engelder, T., Geiser, P., 1980. On the use of regional joint sets as trajectories of paleostress fields during the development of the Appalachian Plateau, New York. *J. Geophys. Res. Solid Earth* 85 (B11), 6319–6341.
- Fletcher, R.C., Pollard, D.D., 1981. Anticrack model for pressure solution surfaces. *Geology* 9, 419–424.
- Freeman, B., Quinn, D.J., Dillon, C.G., Arnhild, M., Jaarsma, B., 2015. Predicting subseismic fracture density and orientation in the gorm field, Danish North Sea. *Geol. Soc. Lond. Special Publ.* 421, 231–244.
- Granier, T., 1985. Origin, damping and pattern of development of faults in granite. *Tectonics* 4, 721–737.
- Hafner, W., 1951. Stress distribution and faulting. *Bull. Geol. Soc. Am.* 62, 373–398.
- Hancock, P.L., Engelder, T., 1989. Neotectonic joints. *Geol. Soc. Am. Bull.* 101 (10), 1197–1208.
- Homberg, C., Hu, J.C., Angelier, J., Bergerat, F., Lacombe, O., 1997. Characterization of stress perturbation near major fault zones: insights from 2-D distinct-element numerical modelling and field studies (Jura Mountains). *J. Struct. Geol.* 19, 703–718.
- Homberg, C., Angelier, J., Bergerat, F., Lacombe, O., 2004. Using stress deflections to identify slip events in fault systems. *Earth Planet. Sci. Lett.* 217, 409–424.
- Healy, D., Jones, R.R., Holdsworth, R.E., 2006. Three-dimensional brittle shear fracturing by tensile crack interaction. *Nature* 439 (7072), 64–67.
- Healy, D., Blenkinsop, T.G., Timms, N.E., Meredith, F.G., Mitchell, T.M., Cooke, M.L., 2015. Polymodal faulting: time for a new angle on shear failure. *J. Struct. Geol.* 80, 57–71.
- Laubach, S.E., Olson, J.E., Gross, M.R., 2009. Mechanical and fracture stratigraphy. *AAPG Bull.* 93, 1413–1426.
- Lejri, M., 2015. *Subsurface Stress Inversion Modeling Using Linear Elasticity: Sensitivity Analysis and Applications*. Ph.D. thesis, Montpellier University.
- Lejri, M., Maerten, F., Maerten, L., Soliva, R., 2015. Paleostress inversion: a multi-parametric geomechanical evaluation of the Wallace-Bott assumptions. *Tectonophysics* 657, 129–143.
- Lisle, R.J., Orife, T.O., Arlegui, L., Liesa, C., Srivastava, D.C., 2006. Favoured states of paleostress in the earth's crust: evidence from fault-slip data. *J. Struct. Geol.* 28, 1051–1066.
- Lisle, R.J., 2013. A critical look at the Wallace-Bott hypothesis in fault-slip analysis. *Bull. la Société Géologique Fr.* 184 (4–5), 299–306.
- Lorenz, J.C., Finley, S.J., 1991. Regional fractures II: fracturing of Mesaverde reservoirs in the Piceance basin, Colorado. *AAPG Bull.* 75 (11), 1738–1757.
- Maerten, L., 1999. *Mechanical Interaction of Intersecting Normal Faults: Theory, Field Examples and Applications*. Ph.D. thesis, Stanford University.
- Maerten, L., 2000. Variation in slip on intersecting normal faults: implications for paleostress inversion. *J. Geophys. Res. Solid Earth* 105, 25553–25565.
- Maerten, L., Pollard, D.D., Gillespie, P., 2002. Effects of local stress perturbation on secondary fault development. *J. Struct. Geol.* 24, 145–153.
- Maerten, L., Gillespie, P., Daniel, J.-M., 2006. 3-D geomechanical modeling for constraint of subseismic fault simulation. *Am. Assoc. Petroleum Geol.* 90, 1337–1358.
- Maerten, F., Maerten, L., Cooke, M.L., 2010. Solving 3D boundary element problems using constrained iterative approach. *Comput. Geosci.* 14, 551–564.
- Maerten, F., 2010a. Adaptive cross-approximation applied to the solution of system of equations and post-processing for 3D elastostatic problems using the boundary element method. *Eng. Analysis Bound. Elem.* 34, 483–491.
- Maerten, F., 2010b. *Geomechanics to Solve Geological Structure Issues: Forward, Inverse and Restoration Modeling*. Ph.D. thesis, University of Montpellier II.
- Maerten, F., Maerten, L., Pollard, D.D., 2014. iBem3D, a three-dimensional iterative boundary element method using angular dislocations for modeling geologic structures. *Comput. Geosciences* 72, 1–17.
- Maerten, F., Madden, B., Pollard, D.D., Maerten, L., 2016. Incorporating Fault Mechanics into Inversions of Aftershock Data for the Regional Remote Stress, with Application to the 1992 Landers, California Earthquake, 674, 52–64.
- Mollema, P.N., Antonellini, M.A., 1996. Compaction bands: a structural analog for anti-mode I cracks in aeolian sandstone. *Tectonophysics* 267, 209–228.
- Muller, O.H., Pollard, D.D., 1977. The stress state near Spanish Peaks, Colorado determined from a dike pattern. *Pure Appl. Geophys.* 115, 69–86.
- Nemčok, M., Gayer, R., Miliorizos, M., 1995. Structural analysis of the inverted Bristol Channel Basin: implications for the geometry and timing of fracture porosity. *Geological Society of London. Spec. Publ.* 88, 355–392.
- Nemčok, M., Lisle, R.J., 1995. A stress inversion procedure for polyphase fault/slip data sets. *J. Struct. Geol.* 17, 1445–1457.
- Nieto-Samaniego, A.F., Alaniz-Alvarez, S.A., 1995. Influence of the structural framework on the origin of multiple fault patterns. *J. Struct. Geol.* 17, 1571–1577.
- Peacock, D.C.P., Sanderson, D.J., 1992. Effect of layering and anisotropy on fault geometry. *J. Geol. Soc. Lond.* 149, 793–802.
- Petit, J.-P., Mattauer, M., 1995. Palaeostress superimposition deduced from meso-scale structures in limestone: the Matelles exposure, Languedoc, France. *J. Struct. Geol.* 17, 245–256.
- Petit, J.-P., Wibberley, C.A.J., Ruiz, G., 1999. 'Crack-seal, slip': a new fault valve mechanism? *J. Struct. Geol.* 21, 1199–1207.
- Petit, J.-P., Auzias, V., Rawnsley, K.D., Rives, T., 2000. Development of joint sets in association with faults. In: Lehner, F.K., Urai, J.L. (Eds.), *Aspects of Tectonic Faulting – in Honour of Georg Mandl*. Springer, Berlin, pp. 167–183.
- Pollard, D.D., Aydin, A.A., 1988. Progress in understanding jointing over the past

- century. *Geol. Soc. Am. Bull.* 100, 1181–1204.
- Pollard, D.D., Saltzer, S.D., Rubin, A.M., 1993. Stress inversion methods: are they based on faulty assumptions? *J. Struct. Geol.* 15, 1045–1054.
- Pollard, D.D., Segall, P., 1987. Theoretical displacements and stress near fractures in rocks: with applications to faults, joints, veins, dikes, and solution surfaces. In: Atkinson, B.K. (Ed.), *Fracture Mechanics of Rock*. Academic Press, London, pp. 277–349.
- Rawnsley, K.D., Rives, T., Petit, J.-P., Hencher, S.R., Lumsden, A.C., 1992. Joint development in perturbed stress fields near faults. *J. Struct. Geol.* 14, 939–951.
- Rawnsley, K., Auzias, V., Petit, J.-P., Rives, T., 1997. Extrapolating fracture orientations from horizontal wells using stress trajectory models. *Pet. Geosci.* 3, 145–152.
- Rawnsley, K.D., Peacock, D.C.P., Rives, T., Petit, J.-P., 1998. Joints in the Mesozoic sediments around the Bristol Channel basin. *J. Struct. Geol.* 20, 1641–1661.
- Rispoli, R., 1981. Stress fields about strike-slip faults inferred from stylolites and tension gashes. *Tectonophysics* 75, 29–36.
- Soliva, R., Maerten, F., Petit, J.-P., Auzias, V., 2010. Field evidences for the role of static friction on fracture orientation in extensional relays along strike slip faults: comparison with photoelasticity and 3-D numerical modelling. *J. Struct. Geol.* 32, 1721–1731.
- Taha, M., 1986. Apport de la microtectonique cassante au problème des trajectoires de contraintes et de leurs perturbations. Exemples du Nord de Montpellier. Ph.D. thesis. Université de Montpellier II.
- Thomas, A.L., 1993. Poly3D, a Three-dimensional, Polygonal-element, Displacement Discontinuity Boundary Element Computer Program with Applications to Fractures, Faults, and Cavities in the Earth's Crust. M.S. thesis. Stanford University.
- Watkinson, A.J., Ward, E.M.G., 2006. Reactivation of pressure-solution seams by a strike-slip fault-sequential, dilatational jog formation and fluid flow. *AAPG Bull.* 90, 1187–1200.